

Technology

Long-term time-lapse multimodal intravital imaging of regeneration and bone-marrow-derived cell dynamics in skin

Benedikt W. Graf^{1,2}, Eric J. Chaney¹, Marina Marjanovic¹, Steven G. Adie¹, Michael De Lisio^{1,3}, M. Carmen Valero¹, Marni D. Boppart^{1,3} & Stephen A. Boppart^{1,2,4}

A major challenge for translating cell-based therapies is understanding the dynamics of cells and cell populations in complex *in vivo* environments. Intravital microscopy has shown great promise for directly visualizing cell behavior *in vivo*. However, current methods are limited to relatively short imaging times (hours), by ways to track cell and cell population dynamics over extended time-lapse periods (days to weeks to months), and by relatively few imaging contrast mechanisms that persist over extended investigations. We present technology to visualize and quantify complex, multifaceted dynamic changes in natural deformable skin over long time periods using novel multimodal imaging and a non-rigid image registration method. These are demonstrated in green fluorescent protein (GFP) bone marrow (BM) transplanted mice to study dynamic skin regeneration. This technology provides a novel perspective for studying dynamic biological processes and will enable future studies of stem, immune, and tumor cell biology *in vivo*.

INNOVATION

The technological innovations presented in this study are highly enabling, and overcome major limitations in imaging the dynamics of cells and cell populations *in vivo*. To expand image information content by way of multiple contrast mechanisms, an integrated, multimodal microscope system is used to provide spatially co-registered image data from multiple structural, functional, and molecular optical imaging modalities. The multimodal microscope features three-dimensional co-registered two-photon excited fluorescence (TPEF), second harmonic generation (SHG), and structural and microvascular optical coherence tomography (OCT) imaging, which enable BM-derived cells and their microenvironments to be visualized *in vivo*. Unique to enable long-term, time-lapse imaging, a novel non-rigid registration algorithm and approach was developed, demonstrated, and quantitatively evaluated for deformable skin tissues, for imaging cell dynamics, and for several wound healing and skin regeneration processes over a period of several months, including collagen synthesis, angiogenesis, structural repair, and wound contraction biomechanics.

INTRODUCTION

Intravital imaging technology has enabled key insights in cell biology research, particularly in the area of immunology for understanding the dynamic behavior of immune cells¹. Despite this success, the application of this technology to a broader range of research areas is hampered by several challenges. Compared to *in vitro* environments, such as 2D culture plates, *in vivo* tissue consists of many interconnected

cellular and extracellular components which interact to influence the biological process under study. The generation of sufficient contrast to provide a comprehensive view of these tissue components *in vivo* represents a significant technical challenge. Although several optical imaging modalities have been developed that are suitable for *in vivo* imaging of intact tissue, such as reflectance confocal microscopy², two-photon excited fluorescence (TPEF) microscopy^{3,4}, second harmonic generation (SHG) microscopy⁵ and optical coherence tomography (OCT)⁶, the contrast generated by each modality alone often provides a limited view of the tissue under study. Since many of these imaging techniques rely on different contrast mechanisms, multimodal approaches have the potential to provide a more comprehensive view of tissue^{7–10}.

Multimodal optical imaging techniques including optical coherence microscopy, multiphoton microscopy, and fluorescence lifetime imaging microscopy have previously been used for structural and functional imaging of engineered and natural *in vivo* human skin¹¹. Fast OCT/OCM imaging of *in vivo* human skin has demonstrated the potential for dynamic *in vivo* scattering-based cytometry measurements of individual flowing blood cells within skin capillary loops¹². Protocols have been established for multimodal imaging of skin wounds and BM-derived cell dynamics over a few weeks¹³, as well as to help reveal the presence and contributions of BM-derived cells in skin grafts in murine animal models¹⁴. These earlier studies, however, have not utilized non-rigid image registration approaches across all modalities to enable long-term time-lapse imaging in deformable skin tissue and facilitate the investigation of the complex

¹Beckman Institute for Advanced Science and Technology, ²Department of Electrical and Computer Engineering, ³Department of Kinesiology and Community Health,

⁴Departments of Bioengineering and Internal Medicine, University of Illinois at Urbana-Champaign, 405 N. Mathews Avenue, Urbana, IL 61801, USA. Correspondence should be addressed to S.A.B. (boppart@illinois.edu).

dynamics of wound biomechanics and contraction *in vivo*. The deformable nature of skin, while presenting a challenge for dynamic cell imaging, also presents a potentially diagnostic metric. OCT, optical coherence elastography, and other multimodal optical imaging techniques have also been developed for assessing skin biomechanics with high-resolution^{15,16}.

A significant challenge for *in vivo* imaging studies is the long time scales over which many biological processes, including regeneration and tumorigenesis, occur. The majority of intravital imaging studies are limited to continuous imaging of dynamic events that occur over several hours or less. Algorithms have also been developed for correcting the presence of motion artifacts in real-time microscopy applications¹⁷. Methods for tracking long-term changes in *in vivo* animal experiments have typically been limited to rigid tissues, such as bone marrow^{18,19}, or require the use of surgically implanted imaging windows^{20,21}. To broaden the range of tissues which can be used for such experiments, and to avoid the need for such highly invasive implants, methods for long-term imaging in deformable natural tissue environments are needed. In rigid environments, registration of images between sessions is either not necessary or is limited to a simple rigid registration which only considers a single rotation, scaling and translation²¹. Such approaches are generally not suitable for time-lapse imaging in natural tissue environments that may be highly flexible and deformable, such as skin. The non-rigid changes that can occur between imaging sessions must be accounted for in order to track the same tissue site over several days or months, as well as for separating the small-scale movement and dynamics of single cells from the larger-scale changes due to tissue deformation. Non-rigid registration is commonly used in medical

applications with modalities such as magnetic resonance imaging (MRI) and X-ray computed tomography (CT)²², but have yet to be employed for long-term observation of cellular and tissue dynamics *in vivo*.

In this paper, we demonstrate the ability to visualize and quantify complex, multifaceted dynamic changes during regeneration in skin over long time periods. These methods are based on a multimodal imaging technique combining three-dimensional (3D) TPEF, SHG, structural OCT, and microvascular OCT imaging, in addition to a non-rigid image registration method that utilizes hair follicle positions as landmarks. We utilize these methods for imaging the dynamics of bone marrow (BM) derived cells and their microenvironments during regeneration in green fluorescent protein (GFP) BM transplanted mice over several months. BM-derived cells are known to play a key role in cutaneous regeneration by contributing immune cells during inflammation. Recently, several studies have suggested that BM can also contribute a range of non-inflammatory cell types^{23–28}, such as mesenchymal stem cells²⁵ and keratinocytes^{24,28}. These cells have profound therapeutic potential and there is strong motivation for understanding their regenerative capacity and the factors that influence their recruitment to peripheral tissue.

Much of the evidence of BM cell contribution to skin regeneration comes from studies based on histological analysis of excised tissue^{23–28}. As skin regeneration consists of many different processes occurring simultaneously over many weeks, and even months to years, these methods are greatly limited in that they can only analyze single time points following a wound. Methods for studying the dynamics of BM-derived cells and their microenvironments *in vivo* have the potential to provide new insight into the functional role of

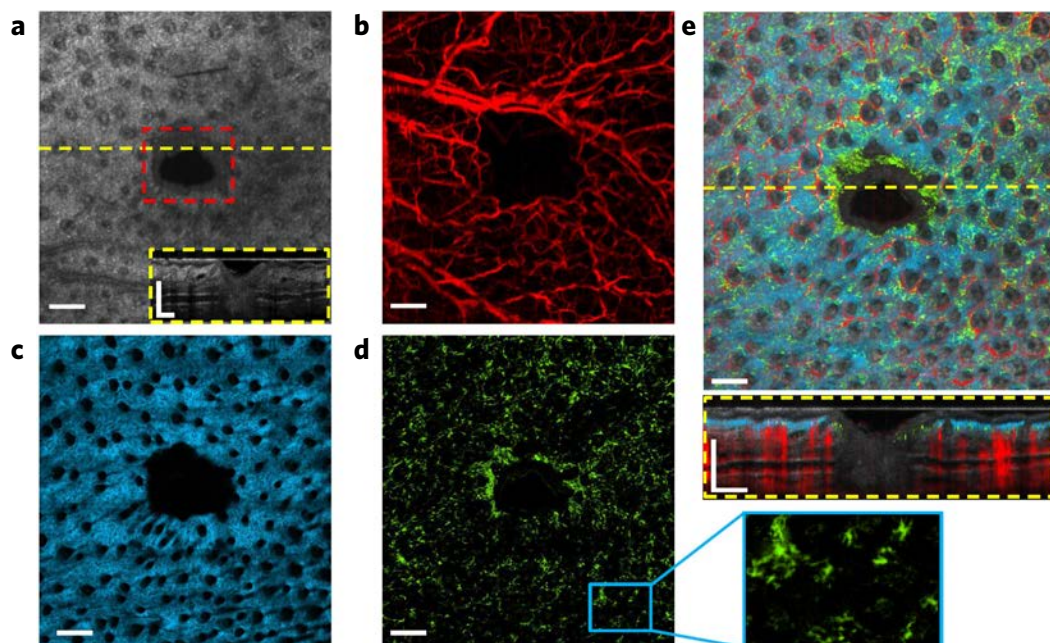


Figure 1 Multimodal imaging of the ear skin in a GFP BM-transplanted mouse 10 days following an excisional wound. **(a)** *En face* structural OCT section showing individual hair follicles and the wound site (red dashed box). Cross-sectional image in the inset shows various layers of the skin at the position of the yellow dashed line. **(b)** Projection of the OCT phase variance volume along the axial dimension showing the microvascular network. **(c)** Wide-area SHG mosaic of collagen. The central dark region represents the wound while the hair follicles appear as smaller dark regions. **(d)** Wide-area TPEF mosaic of the GFP-expressing BM-derived cells in the skin and a magnified view of individual GFP cells. **(e)** *En face* and cross-sectional images of the four modalities overlaid. The cross-sectional image (bottom) was extracted from the 3D volume along the position indicated by the yellow dashed line in **(e)**. Scale bars are 250 μm .

BM cells as well as the conditions under which they can contribute to skin regeneration.

The multimodal imaging technique and long-term imaging methodology presented in this paper allow the dynamics of BM cells to be correlated with various biological processes including structural repair, collagen deposition and remodeling, angiogenesis, and wound contraction. These methods provide novel insight into the dynamic process of BM-derived cell contribution to regeneration and more generally, will enable complex, multifaceted biological process to be visualized *in vivo* for a broad range of applications.

RESULTS

Multimodal skin imaging *in vivo*

We have developed a multimodal microscope which enables co-registered TPEF, SHG, structural OCT and microvascular OCT imaging (Supplementary Fig. 1). We utilized this microscope for *in vivo* 3D imaging of full thickness excisional wounds in the skin of GFP BM transplanted mice. OCT visualizes structural features based on optical scattering properties (Fig. 1a) and is particularly well-suited for resolving the different skin layers, including the epidermis, dermis, and subcutaneous fat. OCT phase variance^{29,30} provides a view of the microvasculature based on the dynamic motion of blood

flow (Fig. 1b). As this method makes use of intrinsic contrast, it provides a significant advantage over other microvascular imaging techniques, such as TPEF, that often require injection of contrast agents (Supplementary Note 1). SHG imaging visualizes the collagen matrix in the dermis of the skin and provides a view of the individual hair follicles, in addition to the collagen reorganization within the wound (Fig. 1c). TPEF imaging allows individual BM-derived GFP expressing cells to be detected in the skin (Fig. 1d). Two-photon generated auto-fluorescence background from hair shafts is subtracted from volumetric TPEF data using a segmentation procedure (Supplementary Fig. 2).

The combination of these modalities allows a wide range of complementary information about living skin to be obtained non-invasively. While TPEF and SHG provide high resolution details in the upper regions of the skin, OCT provides full thickness imaging of the structure and microvasculature of the skin in murine models. Overlaying these modalities allows the microenvironments of individual GFP cells to be visualized in 3D (Fig. 1e). Most importantly, this multimodal imaging combination is non-invasive and does not require the use of exogenous contrast agents, making it suitable for repeated imaging to observe dynamics that occur during skin regeneration, and in the future, making it possible to perform similar skin imaging studies in humans.

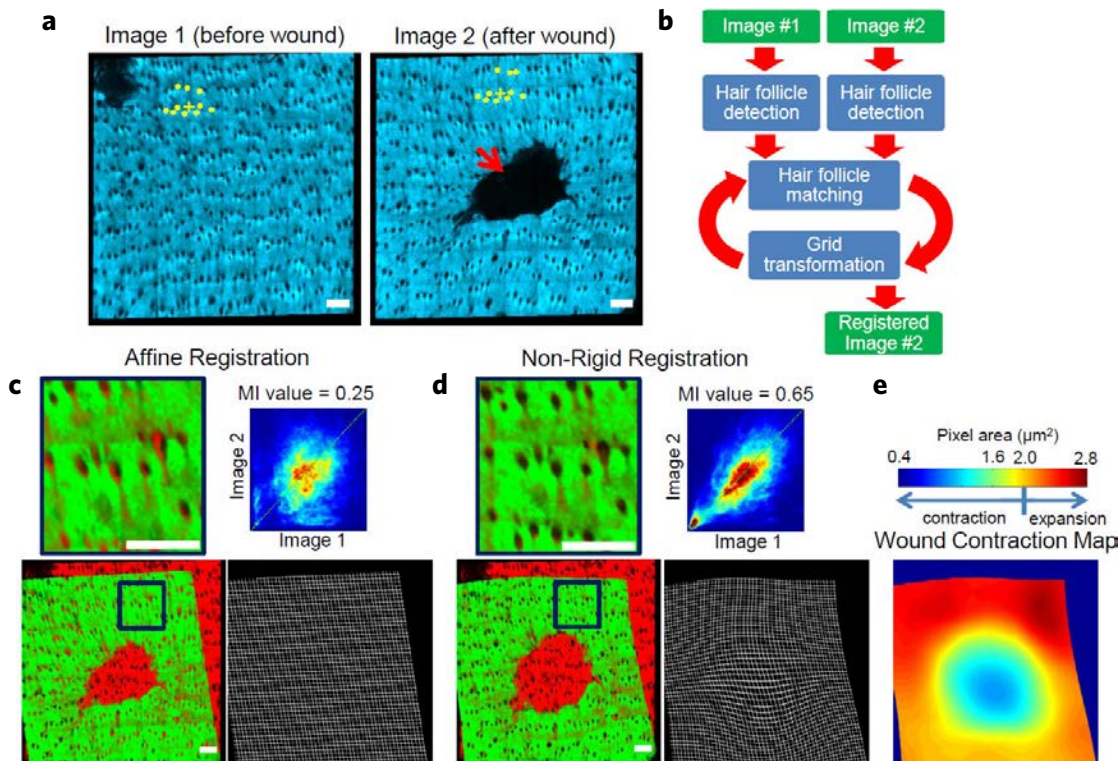


Figure 2 Non-rigid registration of time-lapse skin images based on hair follicle matching. (a) SHG image mosaics of dorsal mouse skin before and 6 hours after a 1.0 mm excisional wound (red arrow). Yellow crosses and dots indicate a pair of corresponding follicles and their closest neighbors, respectively. The spatial patterns of the neighboring hair follicles are used to uniquely identify and match follicles. (b) Block diagram of the registration algorithm. (c,d) Evaluation of affine and non-rigid transformations, respectively. Magnified view of the colored overlays of the mosaics in the region of the dark boxes demonstrates improved alignment of the hair follicles with non-rigid transformation. Improved correlation with the non-rigid transformation is demonstrated quantitatively by the joint histogram and mutual information (MI) metric (top right). The grid images (bottom right) are a representation of the transformed coordinates. (e) Wound contraction map calculated from the non-rigid transformed coordinates showing regions of the wounded skin that have been stretched and contracted between the two time-points. The highly non-rigid nature of the transformation is apparent. Note the dark region in the upper left corner of (a) is the result of an air bubble on the skin surface. It is unrelated to the dark wound region in (b). Scale bars are 250 μm .

Non-rigid registration of time-lapse skin images

The major challenge for long-term tracking of natural wound healing and skin regeneration is that significant mechanical distortions or deformations can occur between imaging sessions. These non-rigid changes are due to both the flexible nature of the skin as well as the contraction of the wound that is inherent during healing. To account for these changes, we have developed a non-rigid registration algorithm that utilizes hair follicles as landmarks. This algorithm exploits the inherent diversity in the spatial patterns of hair follicle positions to uniquely identify and match individual follicles between two images at different time-points. While follicles (as seen in the SHG images) are essentially identical in appearance, their spatial positions relative to neighboring follicles is unique and preserved between imaging sessions (Fig. 2a). Hair follicle regeneration is a relatively rare process³¹, and throughout the extended time-lapse study, there was no detectable change in the number or appearance of the follicles that were used as landmarks. The registration procedure (Fig. 2b) consists of detecting hair follicle positions in the SHG images followed by an iterative procedure of finding hair follicle matches and updating the grid transformation. Once all possible matches are identified, the grid transformation between two images can be utilized to align the images between time points by non-rigid warping.

Non-rigid registration provides a significantly improved alignment of the images compared to simpler methods of registration based on a linear transformation of grid coordinates. Comparing non-rigid transformation with the best approximated affine transformation (Fig. 2c), it is apparent that the affine transformation provides a coarse alignment but fails to accurately align the images on the microscopic scale. Improved alignment between the image subregions in the non-rigid case is quantified by calculating the mutual information (MI) metric from the joint histograms as a measure of the correlation between the images. The extent of the non-rigid mechanical deformation is apparent by calculating the change in pixel area of the transformed image (Supplementary Fig. 3). The resulting deformation map (Fig. 2d) shows areas of the skin after wounding that have been stretched or compressed relative to the reference time point. This demonstrates another significant advantage of performing non-rigid registration, namely the ability to quantitatively assess wound biomechanics, such as contraction, and visualize its spatial arrangement.

Time-lapse imaging of skin regeneration

The combination of multimodal imaging and non-rigid image registration allows several fundamental skin regeneration processes,

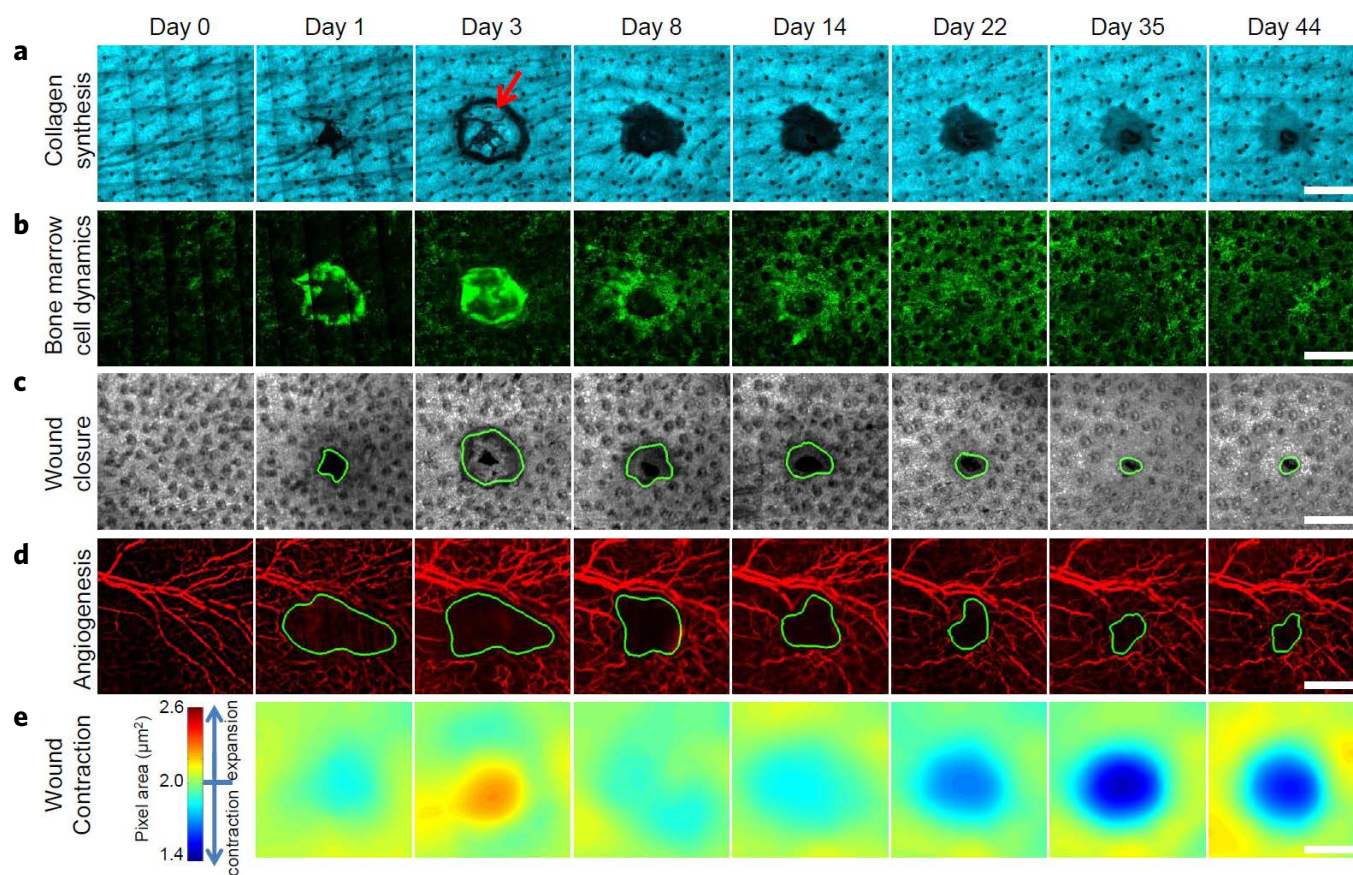


Figure 3 Multimodal, time-lapse sequence of cutaneous wound healing processes. **(a)** Axial projections of the SHG volumes showing scab formation (red arrow) and synthesis of new collagen. **(b)** Axial projections of the TPEF volumes showing the dynamics of the BM-derived, GFP-expressing cell populations. **(c)** *En face* sections from the dermis layer of the structural OCT volume, showing closure of the wound region (area within the green outline). **(d)** Axial projections of the microvascular OCT volume showing the growth of the microvascular network. Area within the green outline indicates region lacking blood vessels. **(e)** Wound contraction maps calculated relative to the initial time point showing that wound contraction stabilizes by 4 weeks. Scale bars are 500 μm .

in addition to BM-derived cell dynamics, to be visualized *in vivo* over a period of several months (Fig. 3, Supplementary Video 1³). Following a $\sim 250\ \mu\text{m}$ excisional wound made in the ear skin of a GFP BM transplanted mouse, multimodal imaging was performed periodically at the same skin site. Non-rigid registration of the time-lapse images corrected mechanical distortions between time points, enabling visualization and quantification of dynamic changes during the entire image sequence.

The sequence of SHG images (Fig. 3a) shows the formation of a scab from the injured skin regions following wounding. Following the natural loss of the scab at Day 8, the SHG signal gradually increases over the remaining weeks as new collagen is synthesized in the wound bed. The population dynamics of the BM-derived GFP cells (Fig. 3b) show two noticeable trends. First, within the wound site, there is initially a dramatic influx of cells, most likely due to inflammatory cells such as neutrophils and macrophages. Many of these cells eventually form part of the scab, giving rise to its strong fluorescence. In the regions surrounding the wound site, the

second noticeable trend is a gradual increase in the cell density which peaks around 3 weeks. While the significance of this trend is not clear, it is important to note that observing such dynamic behavior is a primary advantage of *in vivo* imaging over standard histological methods. In addition to the macroscopic cell population dynamics, distinct cellular morphologies are apparent at different time points (Supplementary Fig. 4) which suggests different functional behavior of the cells or the presence of different cell types contributing to skin regeneration. The OCT structural sequence (Fig. 3c) visualizes the formation of the wound bed and the closure of the wound. The formation and loss of the scab is also apparent. The microvascular OCT sequence (Fig. 3d) demonstrates angiogenesis following the disruption of the microvascular network due to wounding. Finally, the wound contraction sequence (Fig. 3e) demonstrates that the contraction of the wound fully develops between 3–4 weeks. The apparent expansion of the wound at Day 3 in this sequence is an artifact due to the presence of the scab at that time. Over the time period observed, the wound failed to

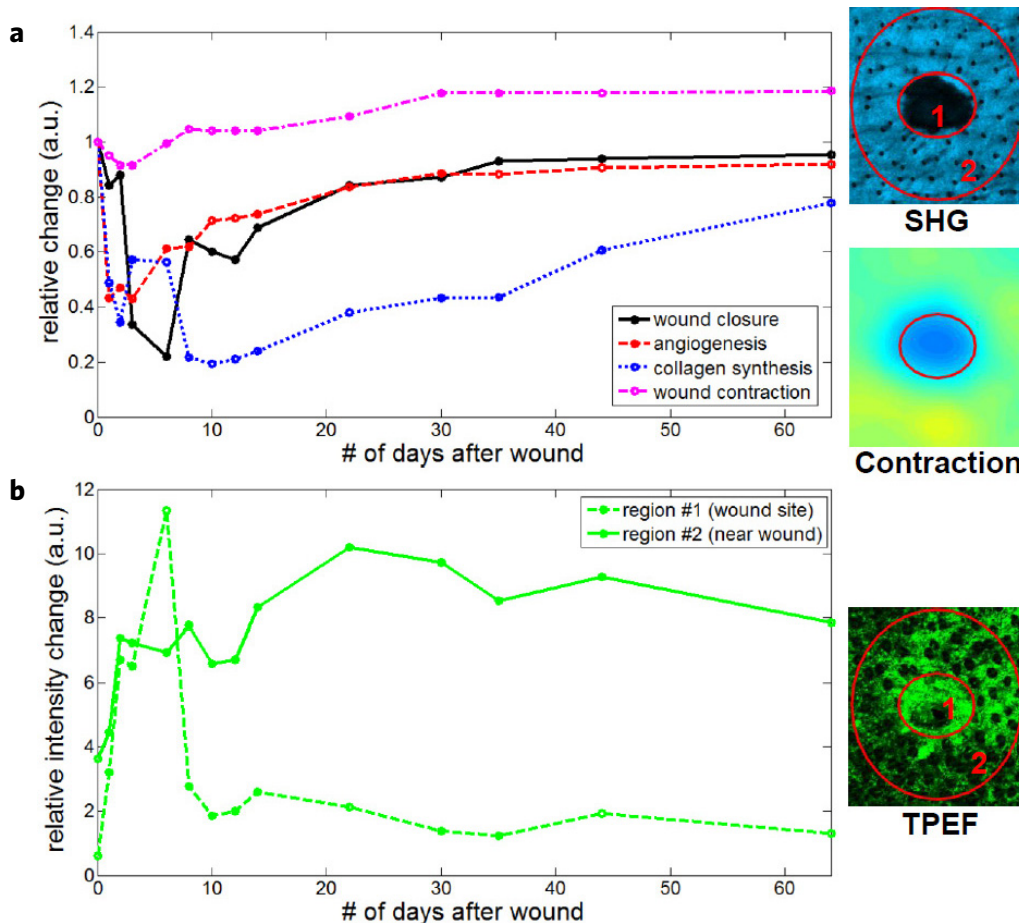


Figure 4 Quantitative analysis of wound healing processes and BM-derived cell population dynamics. (a) Plot of wound closure, angiogenesis, collagen synthesis, and wound contraction as calculated from structural OCT, microvascular OCT, SHG, and non-rigid registration data, respectively (line color corresponds to modality color scales used in Fig. 3). Wound closure and angiogenesis are measured as the relative change in area of the wound size in the structural OCT images and the gap in the microvascular network in the microvascular OCT images, respectively. Collagen content is calculated as the average intensity within region 1 relative to the average intensity in region 2 of the sample SHG image. Contraction of the wound region is measured as the average value within the region shown on the sample contraction TPEF map. (b) Relative measure of GFP cell density based on average signal intensity within and surrounding the wound site (region 1 and 2 in the sample TPEF image, respectively).

³Supplementary Video 1 can be viewed at <http://www.worldscientific.com/doi/suppl/10.1142/S2339547813500027>

heal fully and the contraction remained fully developed. This outcome is likely due to the severity and thickness of the excisional wound.

Quantitative measures of skin regeneration processes (Fig. 4a) and the dynamics of the BM-derived cell populations (Fig. 4b) are calculated from the registered time-lapse image data. TPEF and SHG images are quantified by taking the average signal within manually selected regions of interest throughout the depth of the 3D volumes. Average signal within the wound and a region surrounding the wound is calculated for TPEF and SHG. The average signal within the regions is a relative measure of cell density for TPEF and a relative measure of the collagen content for SHG. The OCT structural and microvascular data are quantified for each time point by manually defining the regions of the wound and the area lacking a microvascular network, respectively. The wound contraction is quantified by taking the average value of the contraction map within the wound region.

Single cell tracking

Individual BM-derived cells in the skin exhibit a range of dynamic temporal behavior (Supplementary Video 2^b). The non-rigid registration method enables tracking of single cell dynamics in a natural skin environment over extended time periods. As continuous intravital microscopy studies of single cell dynamics have been limited by practical considerations to several hours³², this represents a significant and new capability for studying long-term single cell dynamics. Figure 5 demonstrates time-lapse imaging of the activation of a cluster of Langerhans cells (Supplementary Note 2) in the dorsal skin following a full thickness excisional wound in the vicinity. These cells are identified on the basis of their unique morphology and location within the epidermis of the skin³³. A large number of these cells undergo a reorganization of their morphology over a 12 hour time period and migrate from their initial locations

by 24 hours. This is to our knowledge the first *in vivo* time-lapse imaging of the activation of individual Langerhans cells.

DISCUSSION

In this paper we demonstrate long-term time-lapse *in vivo* imaging of complex, multifaceted biological processes in a natural, deformable tissue environment using a multimodal imaging technique and novel non-rigid image registration method. The ability to observe such processes in the same animal represents a significant advantage over previous methods, which require the use of many animals; sacrificing them at various time points for histological analysis. These traditional methods provide an indirect view of long term dynamic changes and are thus prone to errors in interpretation. In addition, histological methods are often limited in the ability to observe multiple features of tissue, and processing wide areas of tissue for many samples can be prohibitively time-consuming. Our methods leverage multimodal, volumetric, non-invasive imaging along with precise co-registration of time-lapse data to enable a novel view of fundamental biological processes in natural tissue environments *in vivo*. This imaging capability complements traditional methods and has the potential to enable new insights into the role and dynamics of BM-derived stem and immune cells during tissue regeneration. In this paper, imaging the skin following cutaneous wound healing in GFP-BM transplanted mice allows several regeneration processes, in addition to BM-derived cell population dynamics, to be simultaneously tracked over a period of several months. These biological processes, which include structural repair, collagen synthesis and reorganization, angiogenesis, mechanical tissue contraction, and cell dynamics, are relevant for other research applications beyond skin regeneration. For example, remodelling of collagen³⁴ and angiogenesis³⁰ are also critical dynamic events in tumor development that occur over long time periods.

A key requirement for visualizing dynamic changes *in vivo* is that the imaging techniques must be non-invasive. The combination

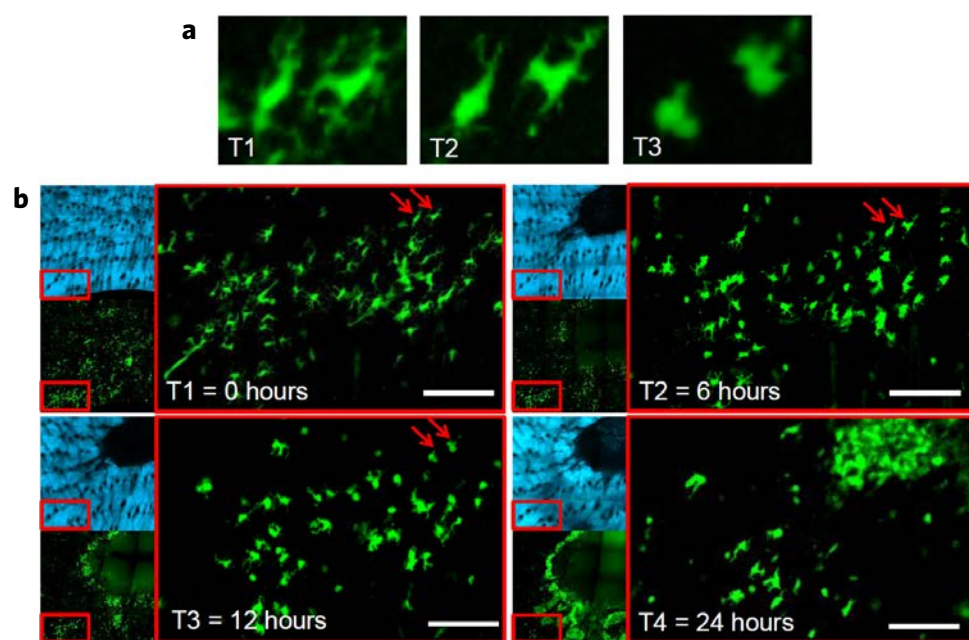


Figure 5 Time-lapse imaging of Langerhans cells, showing their activation over 24 hours following a cutaneous wound located approximately 300 μm away. (a) High magnification TPEF images of the two cells indicated by the red arrows in (b) showing the change in morphology during their activation in the first three time points. The morphology transforms from having many extensions for sensing the extracellular environment for antigens to an amorphous shape suitable for migration. (b) Magnified views of the cell clusters indicated by the red boxes in the wide-area SHG and TPEF images, showing the morphological change and eventual disappearance of many of the Langerhans cells in response to the wound. This behavior is consistent with the known function of Langerhans cells and suggests that many of the cells have migrated from the skin to the lymph nodes. Scale bars are 150 μm.

^bSupplementary Video 2 can be viewed at <http://www.worldscientific.com/doi/suppl/10.1142/S2339547813500027>

of TPEF, SHG, structural OCT, and microvascular OCT imaging of skin used in this study attempts to maximize the use of available intrinsic contrast. Compared to any modality alone, this multimodal approach provides a significantly more comprehensive view of the skin and the dynamic changes occurring at the cellular level. The non-rigid registration method presented in this paper enables tracking of long-term dynamics in natural skin in the presence of significant mechanical deformations. While the algorithm presented is based on matching local patterns of hair follicles in skin, the general principles are suitable for other tissue types which have repeatable structural features (such as colonic crypts or rods and cones in the retina). Due to the inherent challenges of *in vivo* time-lapse microscopy, a majority of intravital imaging studies have focused on short term cell dynamics over a period of hours³⁵. Tracking long-term dynamic changes has been limited to rigid tissues^{18,19} or surgically implanted imaging windows^{20,21}. Non-rigid registration improves the feasibility of time-lapse imaging in a broader range of soft, deformable, tissue types. In conclusion, the multimodal time-lapse imaging methods presented in this paper are powerful tools which promise to broaden the range of applications for intravital imaging in cell biology research. These methods will also facilitate the study of stem, immune, and tumor cell behavior *in vivo*, and ultimately will not only drive new biological discovery, but will also enable translation of diagnostic and therapeutic approaches to clinical applications.

ACKNOWLEDGEMENTS

We gratefully acknowledge the contributions from Darold Spillman, who provided administrative and information technology support related to this research. This research was supported in part by grants from the National Science Foundation (CBET 08-52658 ARRA and CBET 10-33906, S.A.B.). B.W.G. was supported by the Pre-doctoral National Institutes of Health Environmental Health Sciences Training Program in Endocrine, Developmental, and Reproductive Toxicology at the University of Illinois at Urbana-Champaign. M.D. was supported by a CIHR Canada Graduate Scholarship.

AUTHOR CONTRIBUTIONS

S.A.B. had full access to all of the data in the study and takes full responsibility for the integrity of the data and the accuracy of the data analysis. Study concept and design, B.W.G., M.M., M.D.B., S.A.B.; Animal protocols, handling, and procedures, E.J.C., M.D., M.C.V.; Optical system design and development, B.W.G., S.G.A.; Algorithms, software, and system control, B.W.G.; Data acquisition and processing, B.W.G.; Data analysis, B.W.G., E.J.C., M.M., S.G.A., S.A.B.; Drafting of manuscript, B.W.G.; Revisions and review of manuscript, B.W.G., E.J.C., M.M., S.G.A., M.D.L., M.D.B., S.A.B.; Obtained funding, M.D.B., S.A.B.

COMPETING INTERESTS STATEMENT

All authors declare that they have no competing interests.

MATERIALS AND METHODS

Multimodal microscope

The multimodal microscope was a custom-built integrated multiphoton microscope (MPM) and optical coherence tomography (OCT) system. The schematic of the microscope is shown in **Supplementary Fig. 1a**. The system uses a dual spectrum laser

source based on a tunable titanium:sapphire laser (Mai Tai HP, Spectra Physics) which has been previously reported³⁶. The narrowband laser beam was split into two portions, one used for MPM directly and the other for OCT following spectral broadening via supercontinuum generation in a photonic crystal fiber³⁷. For maximal excitation of GFP, the center wavelength of the laser was set to 920 nm, resulting in a 90 nm bandwidth in the supercontinuum broadened beam. The spectral-domain OCT system was based on a free-space interferometer and a custom-built spectrometer in the detection arm. The MPM and OCT beams were recombined in the sample arm with a polarizing beam splitter and focused in the sample with an objective lens. Two galvanometer scanning mirrors and two relay telescopes enabled raster scanning of the laser beam across the sample. A dichroic mirror diverted the TPEF and SHG signals from the sample, which were subsequently detected by a pair of photo-multiplier tubes (PMTs).

TPEF/SHG and OCT datasets were acquired sequentially. The sample arm optics located within the dashed box in **Supplementary Fig. 1a** were interchangeable for switching between high numerical aperture (NA) for TPEF and SHG and low NA for OCT. The detrimental effect of significant coherence curvature was also corrected computationally³⁸. TPEF and SHG images were acquired simultaneously using ~3.5X beam expanding telescope and a 0.95 NA objective lens (XLUMP20X, Olympus). The axial and transverse resolution for TPEF and SHG was 0.8 μm axial and 0.5 μm , respectively. Single images consist of 256 by 256 pixels and the field of view was typically 380 μm . A motorized stage enabled the acquisition of wide-area mosaics. For OCT, a 1X telescope was used with a 40 mm focal length achromatic objective lens, giving an approximate NA of 0.05.

Multimodal image acquisition and processing

For multimodal skin imaging, volumetric TPEF/SHG images were acquired with dimensions of 2.1 mm by 2.1 mm by 0.15 mm (*x*, *y*, and *z*, respectively) using the motorized stage to scan in the lateral and axial dimensions. Single frames were acquired in approximately 1.5 seconds. Images were acquired as 7 by 7 frame mosaics which were stitched together in post-processing resulting in 2189 by 2189 pixel images. Volumes consisted of mosaics acquired at 18 depths with 8 μm spacing. Segmentation of auto-fluorescent hair shafts from TPEF volumes (**Supplementary Fig. 2**) was achieved by apply a threshold to the volume, identifying isolated features, and assessing them based on their size, aspect ratio, and length. The inverse of the resulting binary mask was multiplied to the original image volume to remove the hair shafts.

Corresponding volumetric OCT data was acquired with dimensions of 1.9 mm by 1.9 mm by 0.5 mm (*x*, *y*, and *z*, respectively). Single OCT cross-sectional frames, acquired at 15 Hz, consisted of 1500 by 200 pixels in the lateral and axial dimensions, respectively. OCT volumes consisted of 3500 frames acquired as 7 duplicate frames at 500 locations along the second lateral dimension. Structural OCT volumes were generated by averaging the magnitude of the 7 duplicate frames at each transverse position. Microvascular OCT images were generated by computing the complex variance between adjacent frames at each transverse position, as previously reported³⁰.

TPEF/SHG and OCT volumes were aligned by a rigid transformation of the OCT volumes. This initial calibration transformation for the system was performed using a phantom or sample skin data set. Axial offset was determined by a cross-correlation along the

axial dimension between the structural OCT and SHG volumes. OCT volumes were up-sampled by interpolation along the lateral dimension and the TPEF/SHG were up-sampled by interpolation along the axial dimension so all the image volumes had identical sampling along all three dimensions.

Non-rigid registration of time-lapse images

To enable registration of images acquired at different time points, a non-rigid image registration algorithm was developed. The algorithm consisted of multiple steps (Fig. 2b). The first step was the semi-automated detection of the hair follicle locations as seen in the SHG images. A 2D *en face* SHG image from the 3D volume that provided a good view of the hair follicles was chosen. This image was filtered with a difference-of-Gaussian (DOG) kernel to detect features at the scale of the follicles. Local maxima in the DOG image were detected following the application of a threshold. These maximum positions were considered as the center locations of the follicles. Any incorrectly detected positions were removed manually to improve the accuracy of subsequent steps of the algorithm.

After follicles in two images were located, the match quality between each follicle in one image to each follicle in the other image was evaluated. The match quality was based on the spatial locations of a fixed number of neighboring follicles. The similarity between the pairs of neighboring follicles was calculated by computing the average position error between matching neighboring follicles (Supplementary Methods 1). From all the comparisons made, the matching follicles with an average error position below a threshold were used to define an initial transformation between the two images. The transformation was represented by a 2D thin-plate smoothing spline for each of the image dimensions. Following the determination of the initial transformation, new follicle matches were assessed not only on the quality of the match as defined previously, but also on their consistency with the initial transformation. The remaining hair follicles were matched by an iterative procedure that added new follicle matches to the transformation model each time a match was determined.

The transverse coordinates of an image were represented by a 2D array of 2 element vectors containing the pixel coordinates (i.e. $T_o(x, y) = \{a_x, b_y\}$, where x and y represent the pixels in the image and a_x and b_y represent the coordinates of the pixel). The final thin-plate smoothing spline transformation was used to compute the non-rigid warped coordinates, $T_w(x, y)$, of the image from the original coordinates, $T_o(x, y)$. The warped coordinates were used for a 2D cubic interpolation to warp the images from one time point to the reference time point so that they were registered.

Quantitative comparison of registration methods

A comparison of non-rigid and affine transformations between SHG images was demonstrated by a joint histogram and quantified by a mutual information (MI) metric. The joint histogram of identical images results in a diagonal line in the joint plot, indicating perfect correlation. Thus, images with a strong correlation will have a joint histogram that more closely resembles a diagonal line. Mutual information is a metric that measures the dispersion of the joint histogram and is given by the following equation, $MI = \sum_x \sum_y \log_2 \frac{p(x, y)}{p(x)p(y)}$, where $p(x, y)$ is the joint histogram and $p(x)$ and $p(y)$ are the marginal histograms along the x and y dimension, respectively. Images with no correlation have an MI value of 0.

The least-squares affine transformation was calculated from the non-rigid warped coordinates represented in a homogeneous coordinate system (i.e. $T_o(x, y) = \{a_x, b_y, 1\}$). The linear relationship between the original and warped coordinates was given by, $T_w(x, y) = AT_o(x, y)$, where A is a 3×3 matrix representing the affine transformation in a homogeneous coordinate system. The least-squares affine transformation was determined by inverting this relationship.

Calculation of the contraction map

Aligning images between different sessions was achieved by non-rigid warping of one of the images (Supplementary Fig. 3b,c). This process resulted in a deformation of the original coordinates of the image (Supplementary Fig. 3d,e). This deformation can be quantified in order to assess the degree of wound contraction. The non-rigid registration generates a matrix describing the transformation between two image volumes. In addition to registering the images, it is possible to use this transformation matrix to quantify the mechanical distortion that occurred between the time points. This can provide important biomechanical information about the dynamics of wound contraction. The transformation matrix, expressed in spatial coordinates (x, y) , represents the coordinates of the image after registration, relative to the original image coordinates $T_o(x, y)$. The distance between any two coordinates of the image along one dimension can be calculated by taking the difference of the coordinates. To calculate the area of each pixel in the warped image, the differential of (x, y) along the x and y dimensions was multiplied, $Pixel Area = d_x T(x, y) \times d_y T(x, y)$. This process is illustrated for the original and warped coordinates in Supplementary Fig. 3a. The resulting contraction map from the warped coordinates, $T_w(x, y)$ (Supplementary Fig. 3f), shows regions of the skin that had been stretched or compressed, relative to the reference time point.

Bone marrow transplant

All animal procedures were performed under protocols approved by the Institutional Animal Care and Use Committee (IACUC) at the University of Illinois at Urbana-Champaign. Bone marrow was harvested from donor male mice with global GFP expression (C57BL/6-Tg (CAG-EGFP) 10sb/J)³⁹. After sacrificing via CO₂ inhalation, hind limb bones were dissected, cleaned, placed in phosphate buffered solution (PBS), and crushed with a mortar and pestle. The crushed solution was strained with a 40 micron filter and red blood cells were lysed with an ACK lysing buffer then quenched with PBS. Cell concentration was counted and diluted to approximately 7×10^6 cells/ml and kept on ice prior to transplantation. Recipient female C57BL/6 wild-type mice were treated with radiation from a cobalt-60 source (2 doses of 6 GY, administered 4 hours apart). Donor BM cells were transplanted by tail vein injection (150 μ l, 10^6 cells).

Skin preparation, wounding, and *in vivo* imaging

Mice were anesthetized with isoflurane gas. For imaging dorsal skin, animals were first shaved with electric clippers. For both ear and dorsal skin, hair was carefully removed from the region to be imaged using surgical scissors and a stereo microscope. Full thickness excisional wounds were made using either a 1 mm punch biopsy or manually with a fine tipped scalpel. The skin site to be imaged was

placed against a cover slip fixed to a rigid mount (**Supplementary Fig. 1b**). The whole assembly was mounted on a motorized stage for adjusting the focal depth and acquiring wide area mosaics with TPEF and SHG. Wounding and imaging experiments were performed no less than 2 months after the BM-transplantation procedure.

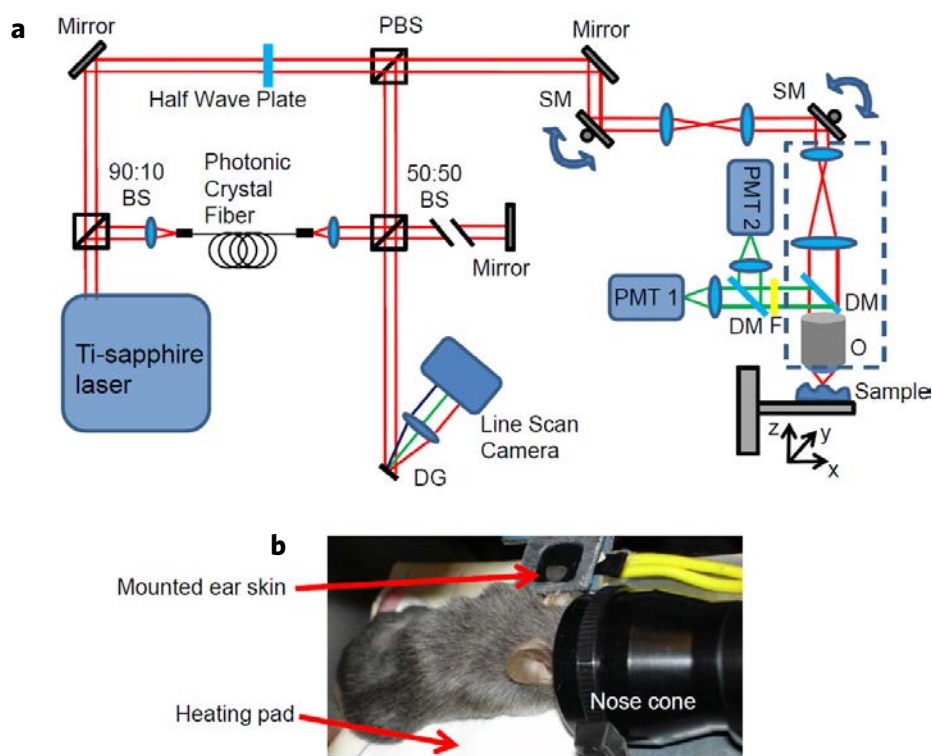
REFERENCES

1. Germain, R.N., Robey, E.A. & Cahalan, M.D. A decade of imaging cellular motility and interaction dynamics in the immune system. *Science* **336**, 1676–1681 (2012).
2. Rajadhyaksha, M., Grossman, M., Esterowitz, D. & Webb, R.H. *In vivo* confocal scanning laser microscopy of human skin: Melanin provides strong contrast. *J. Invest. Dermatol.* **104**, 946–952 (1995).
3. Denk, W., Strickler, J. & Webb, W. Two-photon laser scanning fluorescence microscopy. *Science* **248**, 73–76 (1990).
4. Masters, B.R., So, P.T.C. & Gratton, E. Multiphoton excitation fluorescence microscopy and spectroscopy of *in vivo* human skin. *Biophys. J.* **72**, 2405–2412 (1997).
5. Campagnola, P.J., Wei, M.D., Lewis, A. & Loew, L.M. High-resolution nonlinear optical imaging of live cells by second-harmonic generation. *Biophys. J.* **77**, 3341–3349 (1999).
6. Huang, D. *et al.* Optical coherence tomography. *Science* **254**, 1178–1181 (1991).
7. Beaurepaire, E., Moreaux, L., Amblard, F. & Mertz, J. Combined scanning optical coherence and two-photon-excited fluorescence microscopy. *Opt. Lett.* **24**, 969–971 (1999).
8. Yeh, A.T. *et al.* Imaging wound healing using optical coherence tomography and multiphoton microscopy in an *in vitro* skin-equivalent tissue model. *J. Biomed. Opt.* **9**, 248–253 (2004).
9. Vinegoni, C. *et al.* Integrated structural and functional optical imaging combining spectral-domain optical coherence and multiphoton microscopy. *Appl. Phys. Lett.* **88**, 053901 (2006).
10. Xu, C. *et al.* Spectroscopic spectral-domain optical coherence microscopy. *Opt. Lett.* **31**, 1079–1081 (2006).
11. Zhao, Y. *et al.* Integrated multimodal optical microscopy for structural and functional imaging of engineered and natural skin. *J. Biophotonics* **5**, 437–448 (2012).
12. Graf, B.W. & Boppart, S.A. Multimodal *in vivo* skin imaging with integrated optical coherence and multiphoton microscopy. *IEEE J. Sel. Top. Quantum Electron.* **18**, 1280–1286 (2012).
13. Zhao, Y. *et al.* Imaging and tracking of bone marrow-derived immune and stem cells. *Methods Mol. Biol.* **1052**, 1–20 (2013).
14. Graf, B.W. *et al.* *In vivo* multimodal microscopy for detecting bone-marrow-derived cell contribution to skin regeneration. *J. Biophotonics*. DOI: 10.1002/jbio.201200240 (2013).
15. Liang, X. & Boppart, S.A. Biomechanical properties of *in vivo* human skin by dynamic optical coherence elastography. *IEEE Trans. Biomed. Engr.* **57**, 953–959 (2010).
16. Liang, X., Graf, B.W. & Boppart, S.A. *In vivo* multiphoton microscopy for investigating biomechanical properties in human skin. *Cell. Mol. Bioeng.* **4**, 231–238 (2011).
17. Lorenz, K.S. *et al.* Digital correction of motion artefacts in microscopy image sequences collected from living animals using rigid and nonrigid registration. *J. Microscopy* **245**, 148–160 (2012).
18. Fujisaki, J. *et al.* *In vivo* imaging of T(reg) cells providing immune privilege to the haematopoietic stem-cell niche. *Nature* **474**, 216–219 (2011).
19. Lo Celso, C. *et al.* Live-animal tracking of individual haematopoietic stem/progenitor cells in their niche. *Nature* **457**, 92–96 (2009).
20. Kedrin, D. *et al.* Intravital imaging of metastatic behavior through a mammary imaging window. *Nat. Methods* **5**, 1019–1021 (2008).
21. Perentes, J.Y. *et al.* *In vivo* imaging of extracellular matrix remodeling by tumor-associated fibroblasts. *Nat. Methods* **6**, 143–145 (2009).
22. Crum, W.R., Hartkens, T. & Hill, D.L.G. Non-rigid image registration: Theory and practice. *Br. J. Radiol.* **77**, S140–S153 (2004).
23. Borue, X. *et al.* Bone marrow-derived cells contribute to epithelial engraftment during wound healing. *Am. J. Pathol.* **165**, 1767–1772 (2004).
24. Brittan, M. *et al.* Bone marrow cells engraft within the epidermis and proliferate *in vivo* with no evidence of cell fusion. *J. Pathol.* **205**, 1–13 (2005).
25. Deng, W.M. *et al.* Engrafted bone marrow-derived Flk-1(+) mesenchymal stem cells regenerate skin tissue. *Tissue Eng.* **11**, 110–119 (2005).
26. Fathke, C. *et al.* Contribution of bone marrow-derived cells to skin: Collagen deposition and wound repair. *Stem Cells* **22**, 812–822 (2004).
27. Kataoka, K. *et al.* Participation of adult mouse bone marrow cells in reconstitution of skin. *Am. J. Pathol.* **163**, 1227–1231 (2003).
28. Tamai, K. *et al.* PDGFR alpha-positive cells in bone marrow are mobilized by high mobility group box 1 (HMGB1) to regenerate injured epithelia. *Proc. Nat. Acad. Sci. U.S.A.* **108**, 6609–6614 (2011).
29. Makita, S., Hong, Y., Yamanari, M., Yatagai, T. & Yasuno, Y. Optical coherence angiography. *Opt. Express* **14**, 7821–7840 (2006).
30. Vakoc, B.J. *et al.* Three-dimensional microscopy of the tumor microenvironment *in vivo* using optical frequency domain imaging. *Nat. Med.* **15**, 1219–1223 (2009).
31. Blanpain, C. & Fuchs, E. Epidermal homeostasis: A balancing act of stem cells in the skin. *Nat. Rev. Mol. Cell Biol.* **10**, 207–218 (2009).
32. Phan, T.G. & Bullen, A. Practical intravital two-photon microscopy for immunological research: Faster, brighter, deeper. *Immunol. Cell Biol.* **88**, 438–444 (2010).
33. Kaplan, D.H. *In vivo* function of Langerhans cells and dermal dendritic cells. *Trends Immunol.* **31**, 446–451 (2010).
34. Pietras, K. & Ostman, A. Hallmarks of cancer: Interactions with the tumor stroma. *Exp. Cell Res.* **316**, 1324–1331 (2010).
35. Cavanagh, L.L. & Weninger, W. Dendritic cell behaviour *in vivo*: Lessons learned from intravital two-photon microscopy. *Immunol. Cell Biol.* **86**, 428–438 (2008).
36. Graf, B.W., Jiang, Z., Tu, H. & Boppart, S.A. Dual-spectrum laser source based on fiber continuum generation for integrated optical coherence and multiphoton microscopy. *J. Biomed. Opt.* **14**, 034019 (2009).
37. Tu, H. & Boppart, S.A. Ultraviolet-visible non-supercontinuum ultrafast source enabled by switching single silicon strand-like photonic crystal fibers. *Opt. Express* **17**, 17983–17988 (2009).
38. Graf, B.W., Adie, S.G. & Boppart, S.A. Correction of coherence gate curvature in high numerical aperture optical coherence imaging. *Opt. Lett.* **35**, 3120–3122 (2010).
39. Okabe, M., Ikawa, M., Kominami, K., Nakanishi, T. & Nishimune, Y. 'Green mice' as a source of ubiquitous green cells. *FEBS Lett.* **407**, 313–319 (1997).

SUPPLEMENTARY INFORMATION

Supplementary Figure 1

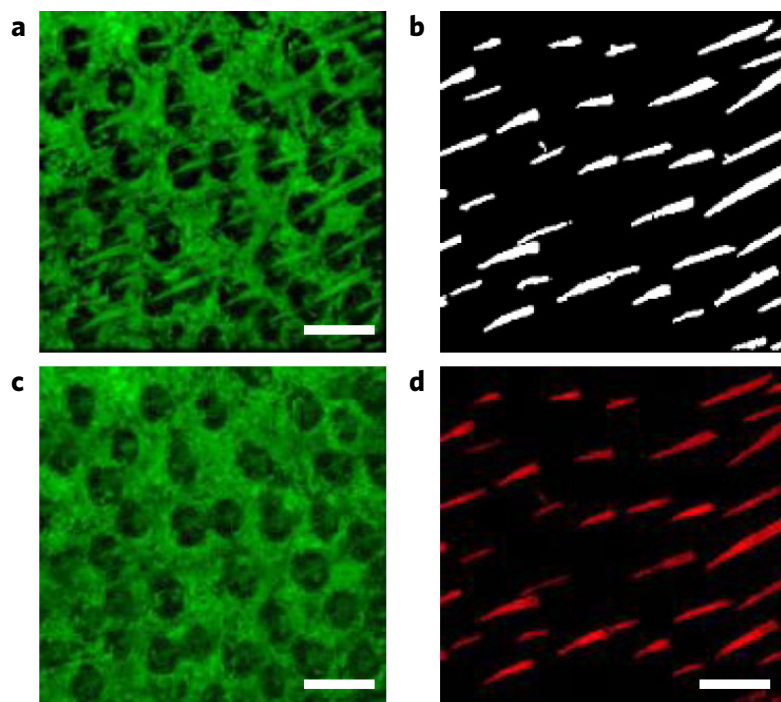
Experimental setup for multimodal *in vivo* imaging.



Supplementary Figure 1 Experimental setup for multimodal *in vivo* imaging. **(a)** Schematic of the multimodal microscope. Abbreviations: BS, beam splitter; DG, diffraction grating; DM, dichroic mirror; F, low-pass filter; O, objective; P, pinhole; PBS, polarizing beam splitter; PMT, photo-multiplier tube; SM, scanning mirror. **(b)** Photo showing placement of the ear skin against a coverslip for imaging.

Supplementary Figure 2

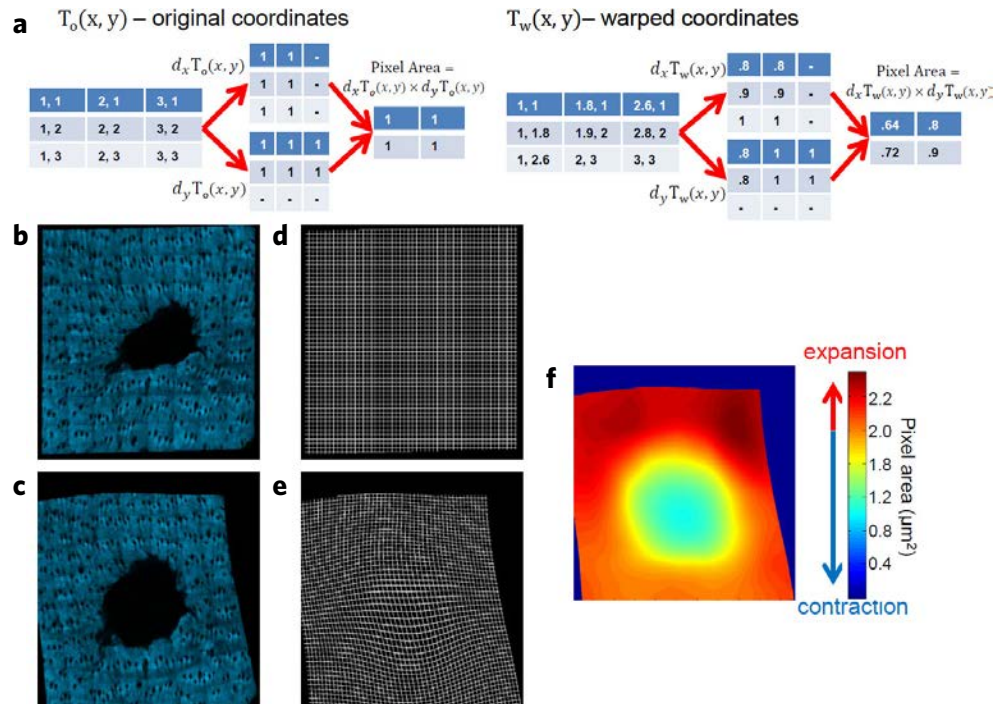
Segmentation procedure for removing autofluorescent hair from 3D TPEF images.



Supplementary Figure 2 Segmentation procedure for removing autofluorescent hair from 3D TPEF images. All images are axial projections of 3D data volume. **(a)** Original TPEF image. **(b)** Binary mask after the hair shaft segmentation procedure. **(c)** TPEF image after removal of the hair shaft features. **(d)** Image of the segmented autofluorescent hair shafts. Scale bars are 200 μm .

Supplementary Figure 3

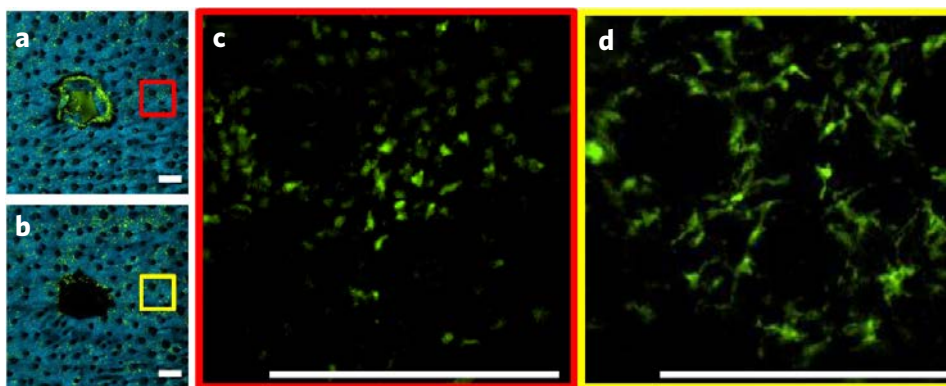
Calculation of wound contraction maps from non-rigid image registration information.



Supplementary Figure 3 Calculation of wound contraction maps from non-rigid image registration information. (a) Illustration of how the original and transformed image coordinates are used to calculate the pixel areas. An SHG skin image (b) before and (c) after warping to correct for non-rigid distortions relative to a reference image. A grid representation of the coordinates of the image (d) before and (e) after warping is evident. (f) The calculated contraction map showing regions of the skin that have contracted and expanded relative to the reference image.

Supplementary Figure 4

Distinct cell morphologies observed at different stages of wound healing.



Supplementary Figure 4 Distinct cell morphologies observed at different stages of wound healing. (a,b) Wide-field SHG/TPEF overlaid images of the ear skin 2 and 12 days following the wound, respectively. (c,d) Higher magnifications of the boxed regions in (a) and (b) showing the TPEF channel only. The distinct morphologies of the BM-derived cells at these two time points is evident and suggests different functional behavior or cell types. Scale bars are 250 µm.

Supplementary Note 1

OCT microvascular imaging versus TPEF. TPEF in combination with intravascular injections of fluorescent contrast agents is a well-known method for imaging blood vessels in small animal experiments. However, the use of contrast agents has numerous disadvantages which are especially problematic in the context of wound healing. Injected contrast agents often leak from the vasculature into peripheral tissue, a problem which would be exacerbated in wounded skin. Leakage of the agent results in degraded contrast between the vasculature and surrounding tissue. Also, repeated injections of the contrast agent required for time-lapse studies present a significant challenge. Microvascular OCT imaging avoids these problems as it is based on intrinsic contrast. In addition, OCT has significantly improved penetration depth when compared to TPEF, allowing the entire depth of the microvascular network in mouse skin to be observed.

Supplementary Note 2

Langerhans cells. Langerhans cells (LC) are a class of dendritic cells whose primary function is to sense the extracellular environment for the presence of antigens^{S1}. These cells reside in the epidermis of the skin and are immobile under steady-state conditions. Upon detection and uptake of antigens, these cells migrate to the lymph nodes to present antigens to other cells in the immune system as part of the adaptive immune response. LCs have a very distinct morphology under steady-state conditions which consists of dendrites which probe the local microenvironment for antigens. Upon activation, these dendritic processes are retracted, resulting in an amorphous morphology that enables migration of the LCs to the lymph nodes. Understanding the functional role of LCs is an active area of research. While these cells were initially thought to play a role in initiating immune responses in reaction to foreign antigens, recent studies have suggested their primary function may be to support immune tolerance^{S1}.

Supplementary Methods 1

Hair follicle match quality for non-rigid image registration. An essential step of the non-rigid registration algorithm was matching hair follicles from two images based on the locations of the neighboring hair follicles. Assessing the match quality between two follicles was based on the following steps.

- For each of the follicles, the positions of a fixed number of the closest points (typically 10–15) were determined. The positions of the closest points were relative to the follicles being compared.
- A local rotation and scaling between the two follicles based on a 2D clustering technique was estimated^{S2}. Rotation and scaling parameters were calculated for each possible match between the neighboring points of the two follicles. The parameters for each matching set of points were plotted in a 2D plane. The correct matches of the neighboring points formed a cluster which was identified based on a peak found in the joint histogram. This method assumed that the local deformation within the range of the neighboring points could be approximated by a rigid transformation.
- One set of neighboring points was rotated and scaled using the estimated parameters. For each neighboring point in one set, its closest match in the other set of neighboring points was identified and the error in position was determined.
- The quality of the match was defined as the average error position between the neighboring points following the local rotation/scaling operation.

SUPPLEMENTARY REFERENCES

- S1. Kaplan, D.H. *In vivo* function of Langerhans cells and dermal dendritic cells. *Trends Immunol.* **31**, 446–451 (2010).
- S2. Chang, S.H., Cheng, F.H., Hsu, W.H. & Wu, G.Z. Fast algorithm for point pattern matching: Invariant to translations, rotations and scale changes. *Pattern Recognit.* **30**, 311–320 (1997).

SUPPLEMENTARY VIDEO**Supplementary Video 1^a****Time-lapse multimodal sequence of wound healing.**

This time-lapse video of the wound healing allows several fundamental wound healing processes to be observed simultaneously *in vivo* over a period of approximately 2 months. The four modalities shown are OCT structural (top left), OCT vascular (bottom left), TPEF (top right) and SHG (bottom right). These modalities visualize structural repair, angiogenesis, bone marrow-derived cell dynamics and collagen synthesis, respectively.

Supplementary Video 2^b**Short-term time-lapse video of bone marrow-derived cell dynamics in skin.**

This video demonstrates the wide range of short-term dynamic behavior exhibited by the GFP labeled bone marrow-derived cells in the dermis of the skin. The video is acquired over a 90 minute time period with 5 minute intervals. Several cells are stationary during this period while other migrate rigorously. Short term dynamics such as this can potentially be used to better understand the functional role of these bone-marrow derived cells.

^{a,b}Supplementary Videos 1 and 2 can be viewed at <http://www.worldscientific.com/doi/suppl/10.1142/S2339547813500027>